# Spin-flop coupling at La$_{0.5}$Sr$_{0.5}$FeO$_3$/La$_{0.7}$Sr$_{0.3}$MnO$_3$ interfaces

Ishmam Nihal [1], Dayne Sasaki [1], Mingzhen Feng [1], Christoph Klewe [2], Padraic Shafer [3],
Andreas Scholl [2], and Yayoi Takamura [1]

[1]*Department of Materials Science and Engineering, University of California, Davis, Davis, California 95616, USA*
[2]*Advanced Light Source, Lawrence Berkeley National Laboratory, Berkeley, California 94720, USA*
[3]*Brookhaven National Laboratory, Upton, New York 11973, USA*

Antiferromagnetic (AFM) spintronics offer several benefits compared to their ferromagnetic (FM) counterparts, such as high storage capacity and faster processing speed, however, difficulties in manipulating and detecting the AFM moments impede their implementation. Spin-flop coupling, the interfacial perpendicular coupling between FM and AFM moments, can be utilized to control the orientation of AFM moments with the application of moderate magnetic fields on the scale of tenths of a Tesla. In this work, epitaxial bilayers of AFM La$_{0.5}$Sr$_{0.5}$FeO$_3$ (LSFO)/FM La$_{0.7}$Sr$_{0.3}$MnO$_3$ (LSMO) with fixed LSMO thickness (∼85 u.c.) and LSFO thicknesses varying from 10 to 50 u.c. were investigated to determine the effect of Sr doping and La$_{1-x}$Sr$_x$FeO$_3$ magnetocrystalline anisotropy on the strength of spin-flop coupling. X-ray magnetic linear dichroism demonstrated that the spin-flop coupling strength decreased with increasing LSFO layer thickness, persisting at a thickness of 50 u.c. (∼20 nm). Furthermore, photoemission electron microscopy revealed a domain-by-domain correlation between the FM and AFM domains consistent with the perpendicular orientation dictated by spin-flop coupling. These results demonstrate that LSFO/LSMO bilayers have the potential to serve as a model materials system for AFM spin transport measurements.

## I. INTRODUCTION

The incorporation of antiferromagnetic (AFM) materials in spintronic devices has the potential to offer several advantages over the use of ferromagnetic (FM) materials, such as high density of magnetic elements inside the device, low power consumption, and faster data processing speed arising from their intrinsic terahertz frequency spin dynamics. However, the net zero magnetization and low susceptibility of AFM materials places great challenges for the manipulation and detection of AFM moments [1]. A way to overcome this difficulty is to harness exchange interactions at FM/AFM interfaces. One type of exchange interaction, referred to as exchange bias, involves the collinear alignment of the interfacial FM and AFM moments and is generally observed if the interfacial AFM moments are uncompensated [2]. Exchange bias is already being used in FM random access memories, where the interfacial AFM moments pin the moments of the reference FM layer, leading to the horizontal shifting of hysteresis loops along the magnetic field axis [3]. A second, less common form of exchange interaction is called spin-flop coupling, where the FM and AFM moments are coupled perpendicular to each other and is observed if the interfacial AFM moments are fully compensated [4,5]. This perpendicular coupling is maintained upon the application of a magnetic field within the plane of the interface, allowing a unique means to reorient the AFM moments indirectly through the exchange interaction with the FM layer.

Robust spin-flop coupling has been observed at (001)-oriented interfaces in the AFM La$_{1-x}$Sr$_x$FeO$_3$/FM La$_{0.7}$Sr$_{0.3}$MnO$_3$ (LSMO) system with Sr doping levels of

$x = 0$ and 0.3 [6–8]. In addition, this effect has been detected in Fe/FeRh bilayers grown on (110)-oriented W substrates, and Fe/NiO bilayers deposited on Cr-buffered (001)-oriented MgO substrates [9,10]. Compared to metallic systems exhibiting spin-flop coupling, perovskite oxide systems offer more tunability of their functional properties arising from the coupling between the spin, charge, orbital, and lattice degrees of freedom, making them promising candidate materials for device applications.

In the presence of spin-flop coupling, the LSMO moments, and consequently the La$_{1-x}$Sr$_x$FeO$_3$ moments, can be reoriented with moderate magnetic fields on the scale of tenths of a Tesla due to the fact that LSMO is a soft ferromagnet [11]. Previously, the spin-flop coupling observed in La$_{0.7}$Sr$_{0.3}$FeO$_3$/LSMO superlattices disappeared once the AFM and FM layer thicknesses reached 18 u.c., suggesting that above a critical thickness, the AFM magnetocrystalline anisotropy energy overcomes the spin-flop coupling strength [7,12]. In the current study, the Sr doping level in the La$_{1-x}$Sr$_x$FeO$_3$ layer was increased to $x = 0.5$ in anticipation of increasing the critical AFM layer thickness beyond which spin-flop coupling vanishes. In undoped LaFeO$_3$, Fe ions have a 3+ valence, leading to AFM ordering of Fe moments via the superexchange interaction along Fe-O-Fe bonds [13]. Sr doping in La$_{1-x}$Sr$_x$FeO$_3$ leads to a proportional increase in the Fe$^{4+}$ ion concentration that disrupts the superexchange mechanism, thereby lowering the Néel temperature [14], and as a result, decreasing the magnetocrystalline anisotropy energy of the AFM La$_{1-x}$Sr$_x$FeO$_3$. In order to minimize the epitaxial strain for both LSMO (pseudocubic lattice parameter, $a_p = 0.3875$ nm [15]) and

La$_{0.5}$Sr$_{0.5}$FeO$_3$ (LSFO) layers ($a_p = 0.3897$ nm [16]), the bilayers were grown on (LaAlO$_3$)$_{0.3}$(SrAl$_{0.5}$Ta$_{0.5}$O$_3$)$_{0.7}$ (LSAT) substrates ($a_p = 0.3868$ nm), thus accounting for the decrease in the pseudocubic lattice parameter of La$_{1-x}$Sr$_x$FeO$_3$ with increasing Sr doping level [16]. As a result, the LSMO and LSFO layers exist under 0.18% and 0.74% compressive strain, respectively, compared to prior studies on SrTiO$_3$ substrates where the LSMO layer was under 0.77% tensile strain, and the La$_{1-x}$Sr$_x$FeO$_3$ layer was under 0.79% compressive strain for $x = 0$, and 0.03% compressive strain for $x = 0.3$ [6–8].

Soft x-ray absorption magnetic spectroscopy demonstrated that spin-flop coupling was maintained at (001) interfaces in LSFO/LSMO bilayers even at a 50 u.c. thickness of the AFM LSFO layer. In addition, x-ray photoemission electron microscopy (X-PEEM) revealed domain-by-domain correlation expected from the perpendicular coupling between FM and AFM moments dictated by spin-flop coupling. These findings in combination with the previous studies provide information about control parameters (Sr doping and epitaxial strain) for spin-flop coupling in La$_{1-x}$Sr$_x$FeO$_3$/LSMO system which is crucial to understand the underlying fundamental mechanism which dictates the spin-flop coupling behavior, and ultimately bring AFM spintronics further closer to becoming a reality.

## II. METHODS

Epitaxial LSFO/LSMO bilayers were deposited on (001)-oriented LSAT substrates by pulsed laser deposition using a KrF laser (248 nm). The substrate temperature was maintained at 710 °C. The LSMO layer (thickness ~85 u.c. or 33 nm) was deposited using a laser fluence of ~1.0 J/cm$^2$ with a laser pulse repetition rate of 1 Hz. Then a fluence of ~2.5 J/cm$^2$ and a repetition rate of 10 Hz were employed to deposit the LSFO layer on top of the LSMO layer (thicknesses of 10, 20, 30, 40, and 50 u.c.). The film thickness was varied by controlling the number of pulses used for each target based on known deposition rates. After the growth, the bilayers were cooled slowly to room temperature in 300 torr of O$_2$ to ensure proper stoichiometry.

The surface roughness and topography of the bilayers were investigated with atomic force microscopy. X-ray reflectivity (XRR) and high-resolution x-ray diffraction (HRXRD) measurements were performed using a Bruker D8 Discover four-circle diffractometer. The XRR and XRD curves were fitted using GenX [17] and LEPTOS [18] software, respectively to characterize the thickness, density, and crystallinity of the thin films. Both Cu $K_{\alpha 1}$ (0.154 06 nm) and $K_{\alpha 2}$ (0.154 44 nm) radiation were used during the XRR analysis, while only Cu $K_{\alpha 1}$ radiation was employed for the HRXRD analysis. The magnetic properties and exchange interactions of the LSFO/LSMO bilayers were probed at 80 K using soft x-ray absorption magnetic spectroscopy at beamline (BL) 4.0.2 of the Advanced Light Source (ALS) at Lawrence Berkeley National Laboratory (LBNL). Two signal detection modes, namely total electron yield (TEY) and luminescence yield (LY), were employed. The current required to compensate for ejected secondary electrons is measured in TEY mode, which leads to its surface sensitivity (within $\lesssim 10$ nm from the sample surface). LY mode utilizes the x-ray excited optical luminescence response of the LSAT substrate and probes
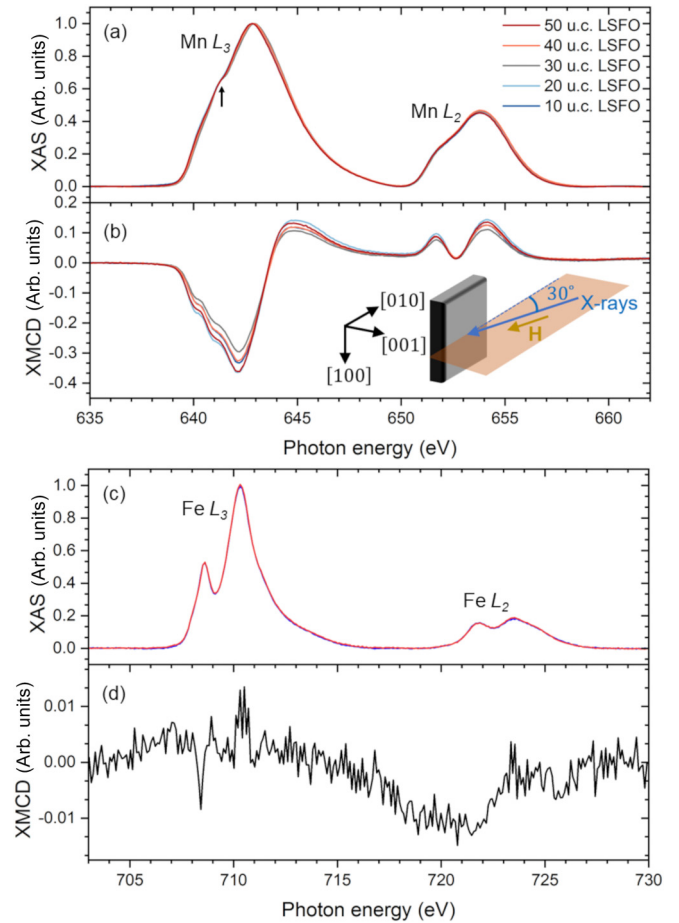


FIG. 1. (a) Mn $L$-edge XA and (b) XMCD spectra of LSFO/LSMO bilayers obtained using LY detection. Experimental geometry is shown in the inset to (b). The coordinate axes indicate substrate crystallographic orientations. (c) Fe $L$-edge XA and (d) XMCD spectra obtained using LY detection from the 10 u.c. LSFO/85 u.c. LSMO bilayer.

the through-thickness sample properties. FM properties were probed using Mn and Fe $L$-edge x-ray magnetic circular dichroism (XMCD) where circularly polarized x rays were incident upon the sample at a 30° grazing incidence angle from the [010] substrate direction and a magnetic field of ±0.3 T was applied parallel to the x-ray beam [see Fig. 1(b)]. XMCD was calculated as the difference between two x-ray absorption (XA) spectra obtained with right/left circularly polarized (rcp/lcp) x rays. AFM properties and the presence of spin-flop coupling were probed using two different geometries of Fe $L$-edge x-ray magnetic linear dichroism (XMLD) measurements. In the first geometry [see Fig. 2(a)], the linearly polarized x rays were incident upon the sample at a 30° grazing incidence angle from the [010] substrate direction. The x-ray $\boldsymbol{E}$ vector was oriented along the in-plane [$\bar{1}$00] substrate direction (*s*-polarized x rays) or canted out-of-plane approximately along the [001] substrate direction (*p*-polarized x rays) and the XMLD spectra were calculated as the difference between XA spectra acquired with $\boldsymbol{E}_{[001]} - \boldsymbol{E}_{[\bar{1}00]}$. The measurements were performed with and without a magnetic field of 0.3 T applied parallel to the x-ray beam. In the second
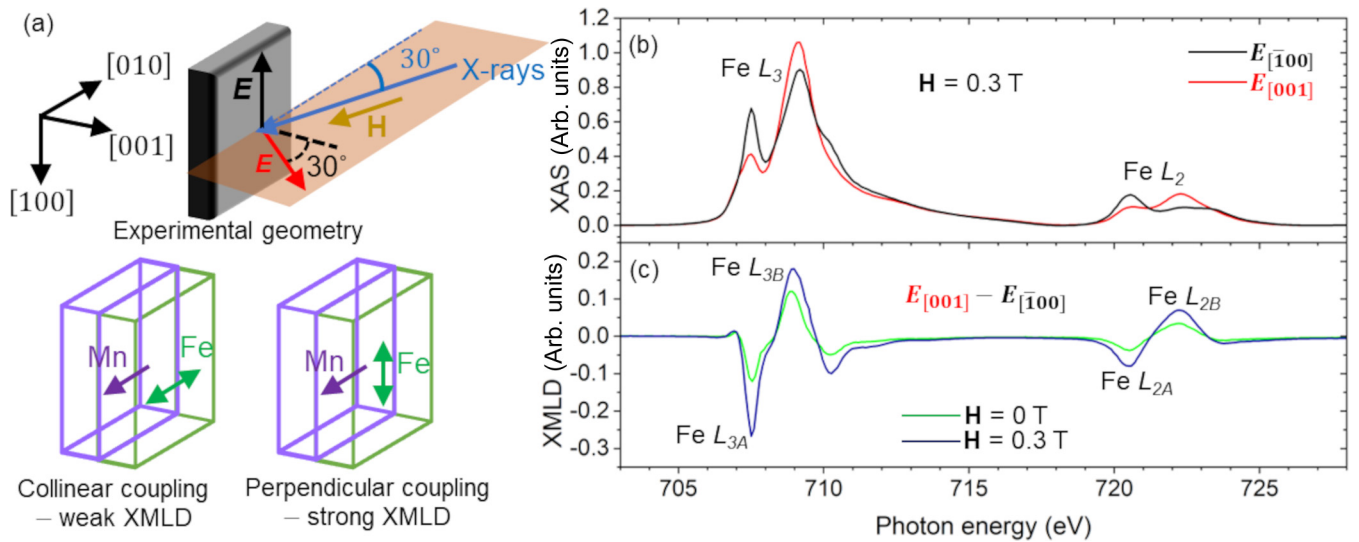
FIG. 2. (a) Experimental geometry for the grazing incidence measurements (the coordinate axes show the substrate crystallographic orientations), and possible coupling (collinear and perpendicular) between FM and AFM moments; black and red arrows denote *s-* and *p*-polarized x rays, respectively, used in the measurements, the gold arrow indicates the applied magnetic field direction, purple and green arrows denote FM and AFM moments, respectively. (b) Fe *L*-edge XA and (c) XMLD spectra obtained using TEY detection for the 10 u.c. LSFO/85 u.c. LSMO bilayer.

geometry [see Fig. 3(a)], the linearly polarized x rays were incident upon the sample at normal incidence and the x-ray $E$ vector was oriented along the in-plane [$\bar{1}$00] and [0$\bar{1}$0] substrate directions. A magnetic field of 0.3 T was applied with a 10° canting angle from the substrate [$\bar{1}$00] direction and the XMLD spectra were calculated as the difference between XA spectra acquired with $E_{[\bar{1}00]} - E_{[0\bar{1}0]}$.

Mn-XMCD hysteresis loops were acquired with rcp/lcp x rays at a fixed x-ray energy corresponding to the maximum Mn $L_3$-edge XMCD intensity and the magnetic field was swept between $+/-$ 0.3 T. Fe-XMLD hysteresis loops were obtained using the grazing incidence geometry [Fig. 2(a)] and the x-ray energy was fixed at the maximum Fe $L_{2B}$-edge XMLD intensity [i.e., the higher photon energy peak in the Fe $L_2$ XMLD signal in Fig. 2(c)] and the magnetic field swept between $+/-$ 0.3 T. At each field, the XMCD and XMLD values were calculated using the formula $|\frac{\text{rcp}-\text{lcp}}{\text{rcp}+\text{lcp}}| \times 100$ and $|\frac{s-p}{s+p}| \times 100$, respectively. For ease of comparison between
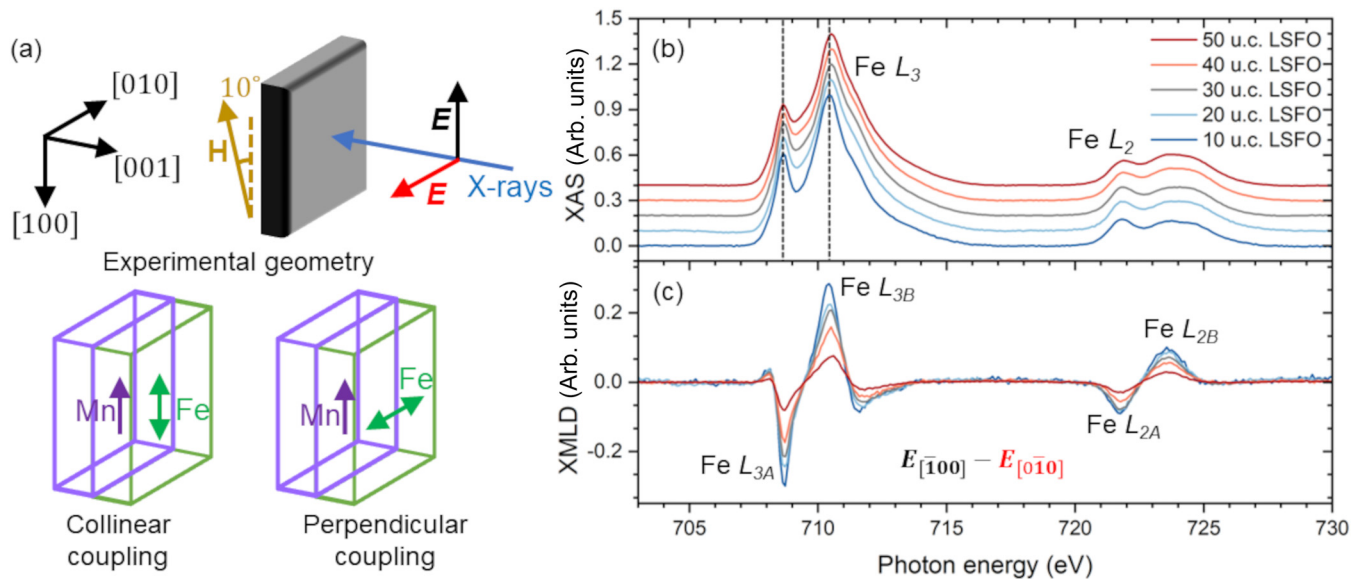


FIG. 3. (a) Experimental geometry for the normal incidence measurements (the coordinate axes show the substrate crystallographic orientations), black and red arrows denote the *s-* and *p*-polarized x rays, respectively used in the measurements, gold arrow indicates the applied magnetic field direction, the purple and green arrows denote FM and AFM moments, respectively. (b) Fe *L*-edge XA and (c) XMLD spectra obtained using LY detection for the LSFO/LSMO bilayers as a function of LSFO thickness.

samples, the hysteresis loops have been plotted as normalized intensity values.

FM and AFM domain images were acquired at 110 K with X-PEEM at BL11.0.1 of the ALS. In this imaging technique, x rays impinged on the sample at a 30° grazing incidence angle from the [010] substrate direction [see Fig. 6(a)]. For FM domain imaging, the x-ray energy was fixed to the maximum Mn $L_3$-edge XMCD intensity, and two images were captured with rcp and lcp x rays. The ratio between these two images isolated the FM contrast from topographical and work function contrast. For AFM domain imaging, two images were captured at the Fe $L_{2A}$ and $L_{2B}$ photon energies (corresponding to the lower/higher photon energy peaks in the Fe $L_2$ XMLD signal) using *s*-polarized x rays where the $\boldsymbol{E}$ vector lies completely on the plane of the sample. An asymmetry calculation was performed on a pixel-by-pixel basis according to $|\frac{L_{2A}-L_{2B}}{L_{2A}+L_{2B}}|$.

## III. RESULTS AND DISCUSSION

### A. Surface morphology and structural properties

Representative 5 μm × 5 μm area atomic force microscopy images of the bilayer samples (see Fig. S1 and Table S1 of the Supplemental Material [19]) demonstrate that the sample surfaces are smooth with surface roughness < 1 nm. Similarly, clear Kiessig fringes are observed in the XRR spectra (see Fig. S2) indicating low interfacial roughness of all the bilayers. Due to the similar chemical densities of bulk LSFO and LSMO ($\sim$6.1 g/cm$^3$ and $\sim$6.4 g/cm$^3$, respectively), Cu $K_\alpha$ x rays cannot distinguish between the LSFO and the LSMO layers, and thus the XRR curves were fit to determine the total bilayer thickness as tabulated in Table S2. Symmetric $\omega$-$2\theta$ XRD scans (see Fig. S3 [19]) show a clear (002) film peak from the thicker LSMO layer and Kiessig fringes, indicating the good crystallinity of the bilayers with smooth interfaces. The peak from the thinner LSFO layers is superimposed on top of the LSMO film peak and Kiessig fringes [19]. The out-of-plane lattice parameters for the LSFO and LSMO layers were determined by fitting the XRD patterns using LEPTOS software [18] and are listed in Table S3 [19]. The LSMO out-of-plane lattice parameter remains constant for all the bilayers, while a weak trend of increasing LSFO out-of-plane lattice parameter with increasing LSFO thickness can be observed. Reciprocal space maps (RSMs) around the asymmetric (103) substrate peak (see Fig. S4) demonstrated that all the LSMO/LSFO bilayers were epitaxially strained to the underlying LSAT substrate as substrate and film pseudocubic (103) peaks share the same $H$ value [19].

### B. Mn and Fe XA and XMCD spectra

The Mn and Fe $L$-edge XA spectra for the LSFO/LSMO bilayers as a function of LSFO layer thickness are shown in Figs. 1(a) and 1(c), respectively, as well as Fig. 3(b), and they denote the valence states and local coordination environment of the Mn and Fe ions in the individual layers. The shoulder feature of the Mn $L_3$-edge XA curves [upward black arrow in Fig. 1(a)] is characteristic of mixed Mn$^{3+}$/Mn$^{4+}$ valence states as expected from the Sr-doping level [20]. The similar shape of all the XA spectra suggests that the Mn valence state

in the LSMO layer ($\sim$85 u.c.) is independent of the LSFO film thickness. Mirroring the XA spectra, the Mn XMCD spectra [Fig. 1(b)] demonstrate that the LSMO layers have similar FM properties regardless of the LSFO layer thickness.

The multiplet structure of the Fe $L$-edge XA spectra [Figs. 1(c) and 3(b)] is indicative of a mixed Fe$^{3+}$ and Fe$^{4+}$ valence state [21]. Figure 3(b) shows that as the LSFO layer thickness increases, the $L_{3B}$ peak shifts towards higher energy by 0.089 eV and both the $L_{3A}$ and $L_{3B}$ peaks become broader, indicating a small increase in Fe$^{4+}$ ion concentration [21]. One possible explanation for this trend is the Mn$^{3+}$ + Fe$^{4+}$ $\rightarrow$ Mn$^{4+}$ + Fe$^{3+}$ charge transfer previously reported at (001)-oriented La$_{0.6}$Sr$_{0.4}$FeO$_3$/La$_{0.6}$Sr$_{0.4}$MnO$_3$ [22] and La$_{0.7}$Sr$_{0.3}$FeO$_3$/LSMO [7] interfaces. The Fe$^{3+}$ ion concentration will appear the highest in the LY signal in the bilayer with the thinnest LSFO layer as the interfacial volume is substantial compared to the total volume of the LSFO layer, and the proportion of this interfacial volume decreases with increasing LSFO layer thickness. The lack of Fe $L$-edge XMCD signal [Fig. 1(d)] indicates the absence of uncompensated Fe moments at the LSFO/LSMO interface.

### C. Fe-XA and XMLD spectra

The presence of spin-flop coupling in LSFO/LSMO bilayers was probed using two different Fe-XMLD geometries [see Figs. 2(a) and 3(a)]. In the absence of a magnetic field, the grazing incidence geometry shown in Fig. 2(a) probes the AFM nature of the LSFO layers as indicated by the nonspherical nature of the electron density around the Fe ions. Due to the cubic symmetry of the LSAT substrate, it is expected that an equal population of AFM domains exists with the AFM Néel vector oriented along the in-plane [100] and [010] directions. For the experimental geometry depicted in Fig. 2(a), the *s*-polarized x rays are parallel to the [100] AFM domains, while *p*-polarized x rays provide sin(30°) and cos(30°) components with the [010] and [001] AFM domains, respectively. As a result, the x-ray linear dichroism (XLD) signal predominantly arises from the [100] AFM domains, while the contribution from [010] AFM domains is proportionally smaller [23]. Figure 2(c) shows that the Fe-XMLD signal for the 10 u.c. LSFO/85 u.c. LSMO bilayer maintains the same spectral shape but increases by a factor of $\sim$2 upon the application of the magnetic field. This result confirms the presence of spin-flop coupling as the magnetic field causes the reorientation of the AFM Néel vector in the [010] domains to the [100] direction, resulting in a single domain AFM state and an increase in the Fe-XMLD intensity. In contrast, if the Fe and Mn moments were collinearly coupled (i.e., [010] AFM domains), then the XMLD signal would change sign compared to the XLD signal.

Fe-XMLD acquisition with the second geometry [Fig. 3(a)] is necessary to prove that spin-flop coupling persists regardless of the orientation of the applied magnetic field. The similar shape of the Fe-XMLD curves from both XMLD geometries [compare Figs. 2(c) and 3(c)] proves the presence of spin-flop coupling because in both cases the XMLD spectrum was calculated as the difference between XA spectra with $\boldsymbol{E} \perp$ AFM axis − $\boldsymbol{E} \parallel$ AFM axis. On the other hand, if the Fe and Mn moments were collinearly
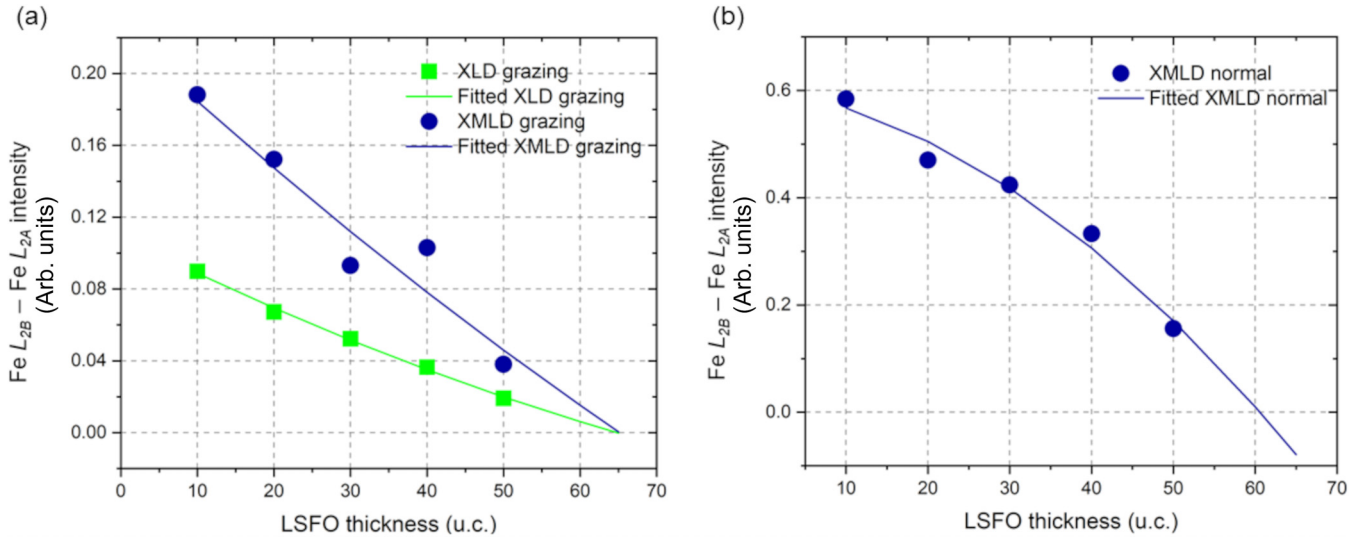
FIG. 4. (a) Fe $L_{2B}$ − Fe $L_{2A}$ XLD and XMLD intensity obtained from the grazing incidence measurement as a function of LSFO thickness, (b) Fe $L_{2B}$ − Fe $L_{2A}$ XMLD intensity obtained from the normal incidence measurement as a function of LSFO thickness.

coupled, the XMLD spectrum would have the opposite sign compared to Fig. 3(c) at both Fe $L_3$ and $L_2$ edges.

To explore the LSFO thickness dependence, Figs. 4(a) and 4(b) plot the maximum XLD and XMLD values at the Fe $L_2$-edge (i.e., Fe $L_{2B}$ − Fe $L_{2A}$) obtained using the grazing incidence [Fig. 2(a)] and normal incidence [Fig. 3(a)] geometries, respectively as a function of LSFO layer thickness. The grazing incidence Fe-XLD and XMLD plots are included in Fig. S5 [19]. As the LSFO thickness increases, the dichroic strength of the XLD/XMLD spectra from both geometries decrease. The decrease in the dichroic strength with increasing LSFO thickness measured in the grazing incidence geometry suggests either (1) an increase in the population of AFM domains with their Néel vector oriented along directions which are not probed in this measurement geometry (i.e., ⟨110⟩ substrate directions or with an out-of-plane canting angle [24,25]) or (2) a decrease in the AFM moment. For the normal incidence XMLD geometry, an additional factor consists of an increase in the magnetocrystalline anisotropy energy of the AFM layer which gradually dominates over the spin-flop coupling strength with increasing thickness. Since the magnetization of ultrathin perovskite oxides have been shown to increase with increasing film thickness [26], case (2) is considered unlikely. The weak change in out-of-plane lattice parameter for the LSFO layer as a function of thickness could be indicative of an evolution of the orientation of the AFM Néel vector and will be the subject of future work. Regardless, spin-flop coupling persists in LSFO/LSMO bilayers even at 50 u.c. LSFO, which surpasses the previously reported critical AFM layer thickness in La$_{0.7}$Sr$_{0.3}$FeO$_3$/LSMO superlattices with lower Sr doping [7]. The data in Fig. 4 were fit with parabolic functions and the fits to both measurement geometries predict that the dichroic strength of the Fe-XLD/XMLD spectra disappear at a common LSFO thickness ∼61 − 65 u.c. The fitting parameters and the associated goodness of the fits are included in Table S4 [19].

## D. XMCD and XMLD hysteresis loops

Further information on the nature of the coupling between the FM and AFM moments in the LSFO/LSMO bilayers can be determined using Mn-XMCD and Fe-XMLD hysteresis loops shown in Fig. 5. Saturating magnetic fields result in a single FM domain configuration, and as a consequence, the spin-flop coupled AFM domains reach a monodomain state to maintain perpendicular relationship with the FM moments, thus the XMCD and XMLD values saturate. At the FM coercive field values, the net magnetization of the FM layer is zero due to formation of domains with their magnetization oriented along their easy directions. The easy magnetization direction of LSMO in these bilayers on LSAT substrates was found to be along ⟨100⟩ directions in this study (see the X-PEEM imaging section). Consequently, spin-flop coupled AFM moments will also be distributed evenly between [100] and [010] domains to maintain their perpendicular orientation, thus the XMLD intensity values will deviate furthest from their saturation values. In Fig. 5, the saturation of XMLD values at positive and negative saturating field of XMCD loops indicates a complete reversal of AFM moments with reversing FM magnetization direction irrespective of LSFO thickness. However, the peaks of the XMLD loops do not coincide precisely with the coercive fields of the XMCD hysteresis loops, but rather lie slightly within the XMCD hysteresis loops (by ∼0.005 T for bilayers with 10 and 20 u.c. LSFO and ∼0.002 T for bilayers with 30 and 40 u.c. LSFO). It was previously reported that the peaks of the XMLD hysteresis loops coincide with the coercive fields of the XMCD loops in spin-flop coupled (111)-oriented interfaces in La$_{0.7}$Sr$_{0.3}$FeO$_3$/LSMO superlattices with 9 and 18 u.c. sublayer thicknesses [27]. Thus, in these LSFO/LSMO bilayers, an even distribution of [100] and [010] AFM domains are achieved by applying fields that are slightly lower than LSMO's coercive field.
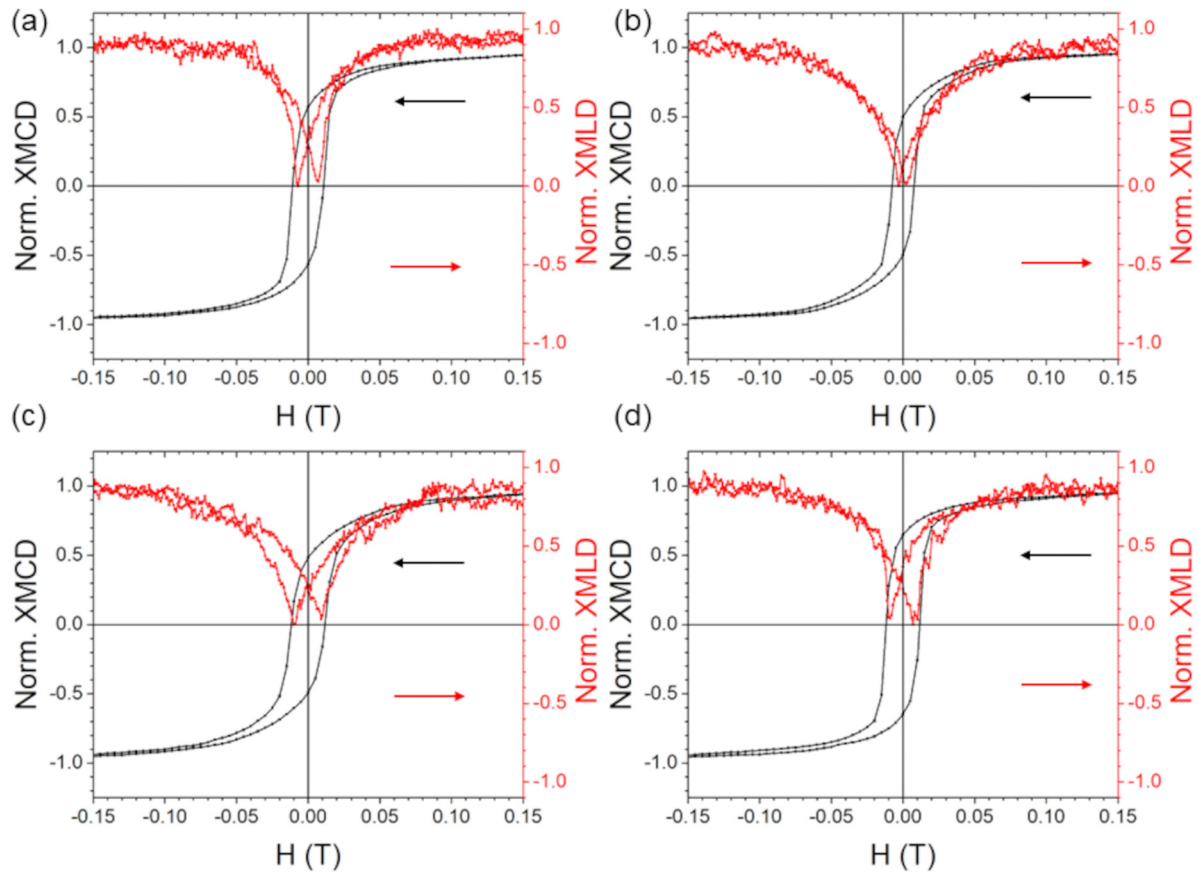
FIG. 5. Normalized Mn-XMCD (black curves) and Fe-XMLD (red curves) hysteresis loops obtained with LY detection from the LSFO/LSMO bilayers with (a) 10 u.c. LSFO, (b) 20 u.c. LSFO, (c) 30 u.c. LSFO, and (d) 40 u.c. LSFO.

### E. X-PEEM imaging

The presence of spin-flop coupling among the FM and AFM domains in the absence of any external magnetic field were investigated using X-PEEM imaging (Fig. 6). The XMCD intensity is proportional to the cosine of the angle between the helicity vector of the circularly polarized x rays
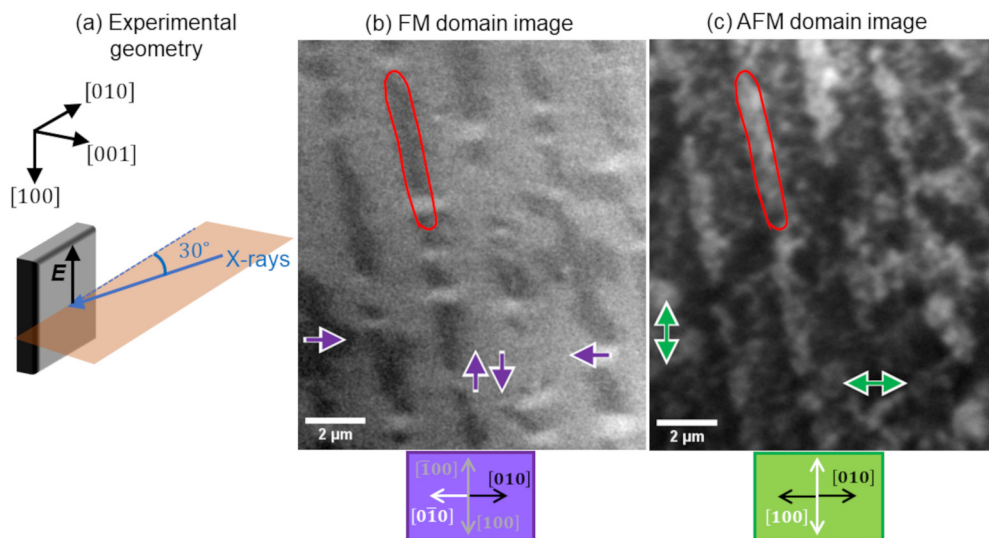


FIG. 6. (a) Experimental geometry; black arrow denotes the orientation of **E** vector of *s*-polarized x rays used for AFM domain imaging (the coordinate axes show the substrate crystallographic orientations). (b) Mn-FM domain image acquired with circularly polarized x rays and (c) Fe-AFM domain image acquired with *s*-polarized x rays for the 20 u.c. LSFO/85 u.c. LSMO bilayer. The purple and green arrows denote FM and AFM moments, respectively. The red lines highlight the correlation between the FM and AFM domains.

and the magnetization vector of the FM domains [28]. Assuming a uniform magnetization throughout the sample, the bright/dark FM domains of Fig. 6(b) have their magnetization vectors parallel/antiparallel to the in-plane projection of the x-ray propagation direction, i.e., the [0$\bar{1}$0] direction, while the magnetization vectors of the gray FM domains are oriented perpendicular to the x-ray propagation direction, along the [100] or [$\bar{1}$00] directions. Figure 6(c) shows the AFM domain image captured using *s*-polarized x rays, where the x-ray **E** vector lies completely in the plane of the sample as shown with the black arrow in Fig. 6(a). The XMLD intensity is proportional to the cosine squared of the angle between the **E** vector and the AFM axis [23]. Therefore, the AFM moments of the bright and dark AFM domains have an in-plane projection along [100] and [010] directions, respectively. Elongated FM domains with alternating dark/bright and gray contrast are observed in Fig. 6(b) with their long axes approximately parallel to the [100] substrate direction. Direct correlation exists between the striped FM and AFM domains shown in Fig. 6. The AFM domains with bright contrast correspond to FM domains with dark/bright contrast while the AFM domains with dark contrast correspond to the FM domains with gray contrast. Therefore, it can be ascertained that the FM and AFM domains maintain the perpendicular orientation as expected for spin-flop coupling.

## IV. CONCLUSION

This study showed the presence of spin-flop coupling at (001)-oriented interfaces of strained LSFO/LSMO bilayers. By increasing the Sr doping from $x = 0.3$ to 0.5 in La$_{1-x}$Sr$_x$FeO$_3$, spin-flop coupling was found to persist beyond a LSFO thickness of 50 u.c. and is predicted to vanish at ∼65 u.c. In contrast, for $x = 0.3$, spin-flop coupling was found to disappear before the La$_{0.7}$Sr$_{0.3}$FeO$_3$ thickness reached 18 u.c. [7]. The strength of spin-flop coupling in LSFO/LSMO bilayers decreased with increasing LSFO thickness, possibly due to the fact that the magnetocrystalline anisotropy strength of the LSFO layer increases with thickness and gradually dominates over spin-flop coupling. Mn $L_{2,3}$ XA spectra revealed that the valence state of the Mn ions and FM properties of the LSMO layer were not affected by the thickness of the AFM LSFO layer. Fe $L_{2,3}$ XA indicated a small increase in Fe$^{4+}$/Fe$^{3+}$ ratio in the AFM layer with increasing LSFO thickness. X-PEEM imaging showed domain-by-domain correlation between the FM and AFM moments dictated by spin-flop coupling. The FM and AFM domains had striped patterns with the long axis oriented along one of the in-plane ⟨100⟩ substrate directions. Understanding of the domain structures and valence states of Mn and Fe ions in spin-flop coupled LSFO/LSMO bilayers together with high critical AFM thickness for spin-flop coupling makes LSFO/LSMO a promising system to conduct spin transport measurements through the AFM layer which is crucial for developing AFM spintronics.

[1] T. Jungwirth, X. Marti, P. Wadley, and J. Wunderlich, Antiferromagnetic spintronics, Nat. Nanotechnol. **11**, 231 (2016).

[2] D. Mauri, H. C. Siegmann, P. S. Bagus, and E. Kay, Simple model for thin ferromagnetic films exchange coupled to an antiferromagnetic substrate, J. Appl. Phys. **62**, 3047 (1987).

[3] S. S. P. Parkin, K. P. Roche, M. G. Samant, P. M. Rice, R. B. Beyers, R. E. Scheuerlein, E. J. O'Sullivan, S. L. Brown, J. Bucchigano, D. W. Abraham *et al.*, Exchange-biased magnetic tunnel junctions and application to nonvolatile magnetic random access memory (invited), J. Appl. Phys. **85**, 5828 (1999).

[4] N. C. Koon, Calculations of exchange bias in thin films with ferromagnetic/antiferromagnetic interfaces, Phys. Rev. Lett. **78**, 4865 (1997).

[5] T. C. Schulthess and W. H. Butler, Consequences of spin-flop coupling in exchange biased films, Phys. Rev. Lett. **81**, 4516 (1998).

[6] E. Arenholz, G. van der Laan, F. Yang, N. Kemik, M. D. Biegalski, H. M. Christen, and Y. Takamura, Magnetic structure of La$_{0.7}$Sr$_{0.3}$MnO$_3$/La$_{0.7}$Sr$_{0.3}$FeO$_3$ superlattices, Appl. Phys. Lett. **94**, 072503 (2009).

[7] Y. Takamura, F. Yang, N. Kemik, E. Arenholz, M. D. Biegalski, and H. M. Christen, Competing interactions in ferromagnetic/antiferromagnetic perovskite superlattices, Phys. Rev. B **80**, 180417(R) (2009).

[8] A. D. Bang, F. K. Olsen, S. D. Slöetjes, A. Scholl, S. T. Retterer, C. A. F. Vaz, T. Tybell, E. Folven, and J. K. Grepstad, Magnetic domain formation in ultrathin complex oxide ferromagnetic/antiferromagnetic bilayers, Appl. Phys. Lett. **113**, 132402 (2018).

[9] P. Dróżdż, M. Ślęzak, K. Matlak, A. Kozioł–Rachwał, J. Korecki, and T. Ślęzak, Spin-flop coupling induced large coercivity enhancement in Fe/FeRh/W(110) bilayers across ferromagnetic–antiferromagnetic phase transition of FeRh alloy, J. Magn. Magn. Mater. **498**, 166258 (2020).

[10] A. Kozioł-Rachwał, M. Ślęzak, M. Zając, P. Dróżdż, W. Janus, M. Szpytma, H. Nayyef, and T. Ślęzak, Control of spin orientation in antiferromagnetic NiO by epitaxial strain and spin–flop coupling, APL Mater. **8**, 060704 (2020).

[11] G. Z. Liu, Y. Y. Yang, J. Qiu, X. X. Chen, Y. C. Jiang, J. L. Yao, M. Zhao, R. Zhao, and J. Gao, Substrate-related structural, electrical, magnetic and optical properties of La$_{0.7}$Sr$_{0.3}$MnO$_3$ films, J. Phys. D: Appl. Phys. **49**, 075304 (2016).

[12] Y. Takamura, Characterization of antiferromagnetic/ferromagnetic perovskite oxide superlattices, in *Nanostructured Materials for Magnetoelectronics*, edited by B. Aktaş and F. Mikailzade, Springer Series in Materials Science Vol. 175 (Springer-Verlag, Berlin, Heidelberg, 2013).

[13] J. B. Goodenough, An interpretation of the magnetic properties of the perovskite-type mixed crystals La$_{1-x}$Sr$_x$CoO$_{3-\lambda}$, J. Phys. Chem. Solids **6**, 287 (1958).

[14] T. Maeder and J. G. Bednorz, Influence of oxygen stoichiometry on electrical transport and magnetic properties of doped

perovskite-type ferrate and manganate single crystals, J. Eur. Ceram. Soc. **19**, 1507 (1999).

[15] O. I. Lebedev, J. Verbeeck, G. Van Tendeloo, C. Dubourdieu, M. Rosina, and P. Chaudouët, Structure and properties of artificial $[(La_{0.7}Sr_{0.3}MnO_3)_m(SrTiO_3)_n]_{15}$ superlattices on (001) $SrTiO_3$, J. Appl. Phys. **94**, 7646 (2003).

[16] A. Fossdal, M. Menon, I. Waernhus, K. Wiik, M. A. Einarsrud, and T. Grande, Crystal structure and thermal expansion of $La_{1-x}Sr_xFeO_{3-\delta}$ materials, J. Am. Ceram. Soc. **87**, 1952 (2005).

[17] A. Glavic and M. Björck, GenX 3: The latest generation of an established tool, J. Appl. Crystallogr. **55**, 1063 (2022).

[18] A. Ulyanenkov, LEPTOS: a universal software for x-ray reflectivity and diffraction, in *Proceedings of SPIE* (SPIE, Bellingham, Washington, USA, 2004), Vol. 5536, pp. 1–15.

[19] See Supplemental Material at http://link.aps.org/supplemental/10.1103/PhysRevB.110.014411 for atomic force microscopy images, XRR, XRD, and RSM data obtained from the samples. It also contains XLD and XMLD data for Fig. 4(a) from the main body text, along with fitting parameters and the goodness of the fits for both Figs. 4(a) and 4(b), which includes Refs. [17,18].

[20] B. Gilbert, B. H. Frazer, A. Belz, P. G. Conrad, K. H. Nealson, D. Haskel, J. C. Lang, G. Srajer, and G. De Stasio, Multiple scattering calculations of bonding and x-ray absorption spectroscopy of manganese oxides, J. Phys. Chem. A **107**, 2839 (2003).

[21] M. Abbate, F. M. de Groot, J. C. Fuggle, A. Fujimori, O. Strebel, F. Lopez, M. Domke, G. Kaindl, G. A. Sawatzky, and M. Takano, Controlled-valence properties of $La_{1-x}Sr_xFeO_3$ and

$La_{1-x}Sr_xMnO_3$ studied by soft-x-ray absorption spectroscopy, Phys. Rev. B **46**, 4511 (1992).

[22] H. Kumigashira, D. Kobayashi, R. Hashimoto, A. Chikamatsu, M. Oshima, N. Nakagawa, T. Ohnishi, M. Lippmaa, H. Wadati, A. Fujimori *et al.*, Inherent charge transfer layer formation at $La_{0.6}Sr_{0.4}FeO_3/La_{0.6}Sr_{0.4}MnO_3$ heterointerface, Appl. Phys. Lett. **84**, 5353 (2004).

[23] J. Stöhr and H. C. Siegmann, X-ray magnetic linear dichroism, in *Magnetism from Fundamentals to Nanoscale Dynamics* (Springer, Berlin, Heidelberg, 2006), pp. 407–415.

[24] E. Folven, A. Scholl, A. Young, S. T. Retterer, J. E. Boschker, T. Tybell, Y. Takamura, and J. K. Grepstad, Effects of nanostructuring and substrate symmetry on antiferromagnetic domain structure in $LaFeO_3$ thin films, Phys. Rev. B **84**, 220410(R) (2011).

[25] M. S. Lee, P. Lyu, R. V. Chopdekar, A. Scholl, S. T. Retterer, and Y. Takamura, Controlling antiferromagnetic domains in patterned $La_{0.7}Sr_{0.3}FeO_3$ thin films, J. Appl. Phys. **127**, 203901 (2020).

[26] R. V. Chopdekar, E. Arenholz, and Y. Suzuki, Orientation and thickness dependence of magnetization at the interfaces of highly spin-polarized manganite thin films, Phys. Rev. B **79**, 104417 (2009).

[27] Y. Jia, R. V. Chopdekar, E. Arenholz, Z. Liu, M. D. Biegalski, Z. D. Porter, A. Mehta, and Y. Takamura, Thickness dependence of exchange coupling in (111)-oriented perovskite oxide superlattices, Phys. Rev. B **93**, 104403 (2016).

[28] J. Stöhr and H. C. Siegmann, Interactions of polarized photons with matter, in *Magnetism From Fundamentals to Nanoscale Dynamics* (Springer, Berlin, Heidelberg, 2006), pp. 385–400.